Front. Struct. Civ. Eng. 2021, 15(4): 1001–1015
https://doi.org/10.1007/s11709-021-0734-8

RESEARCH ARTICLE

Seismic effects on reinforcement load and lateral deformation of geosynthetic-reinforced soil walls

Fei ZHANG[a,b], Yuming ZHU[a,b], Yanbo CHEN[a,b*], Shangchuan YANG[c]

[a] *Key Laboratory of Ministry of Education for Geomechanics and Embankment Engineering, Hohai University, Nanjing 210098, China*

[b] *Jiangsu Province's Geotechnical Research Center, Nanjing 210098, China*

[c] *Key Laboratory of High-speed Railway Engineering of the Ministry of Education, Southwest Jiaotong University, Chengdu 610031, China*

[*] *Corresponding author. E-mail: yanbochen@hhu.edu.cn*

ABSTRACT Current design methods for the internal stability of geosynthetic-reinforced soil (GRS) walls postulate seismic forces as inertial forces, leading to pseudo-static analyses based on active earth pressure theory, which yields unconservative reinforcement loads required for seismic stability. Most seismic analyses are limited to the determination of maximum reinforcement strength. This study aimed to calculate the distribution of the reinforcement load and connection strength required for each layer of the seismic GRS wall. Using the top-down procedure involves all of the possible failure surfaces for the seismic analyses of the GRS wall and then obtains the reinforcement load distribution for the limit state. The distributions are used to determine the required connection strength and to approximately assess the facing lateral deformation. For sufficient pullout resistance to be provided by each reinforcement, the maximum required tensile resistance is identical to the results based on the Mononobe–Okabe method. However, short reinforcement results in greater tensile resistances in the mid and lower layers as evinced by compound failure frequently occurring in GRS walls during an earthquake. Parametric studies involving backfill friction angle, reinforcement length, vertical seismic acceleration, and secondary reinforcement are conducted to investigate seismic impacts on the stability and lateral deformation of GRS walls.

KEYWORDS geosynthetics, reinforced soil, retaining walls, seismic performance

1 Introduction

Geosynthetic-reinforced soil (GRS) walls have been widely used since the 1970s, and many post-construction field investigations [1–5] demonstrate satisfactory performances of GRS walls compared with rigid walls [6,7]. Tatsuoka et al. [8] investigated the performance of Tanata retaining walls after the 1995 Kobe earthquake and found that the Tanata walls produced much smaller horizontal displacement compared with the conventional gravity wall. Obviously, a GRS wall with a rigid facing performs better than the conventional gravity retaining wall. Ling et al. [9] investigated several failures of segmental GRS walls after the 1999 Chi-Chi earthquake and improved the seismic design of GRS walls with flexible facing. The current seismic design method in AASHTO [10] and FHWA [11] postulates seismic effects as internal inertial forces on an active wedge and then follows a procedure based on the static design method. Although both internal and external stability are required for the seismic design of a GRS wall, the scope of the presented analysis is restricted to the internal stability analysis. This study aimed to investigate the effect of seismic forces on the internal stability of GRS walls.

The determination of the reinforcement tensile force required for the internal stability of a GRS wall is significant in its design. Two kinds of calculations on the required tensions are often used for strength limit state

Article history: Received Dec 15, 2020; Accepted Mar 4, 2021

analysis and working stress analysis. Most limit state analyses are based on the Rankine or Coulomb theory of active earth pressure [10–12] and limit equilibrium method [13–15]. The working stress analyses include strain compatibility analysis method [16–18], K-stiffness method [19,20], and numerical methods [21,22] based on finite elements (FEs) or finite difference. However, the seismic stability of a GRS wall is often analyzed at a limit state because of conservative design. Based on the limit equilibrium method, conducting pseudo-static analyses can obtain the maximum required tensile force of the reinforcement. Seismic lateral earth pressure based on the well-known Mononobe–Okabe (M–O) method is often used to determine the internal stability of GRS wall design [23,24]. Instead of the planar failure surface postulated in the M–O method, many studies [25,26] adopted a rotational log-spiral failure surface to obtain the required tensions of the seismic GRS wall. The calculated maximum value of the tensile resistance for each reinforcement layer is used to determine the reinforcement length to ensure sufficient rear-end pullout capacity for internal stability. Considering the complexity of the rotational failure mechanism, the planar failure assumption is more suitable and acceptable for the practical design of seismic GRS walls [27,28].

The lessons [9] learned from the damage of GRS walls during the Chi-Chi earthquake indicate that the possibilities of compound failure and facing connection failure should be extensively acknowledged during seismic design. In fact, the issues are dependent on the distribution of the reinforcement load for each layer. The required distribution would be difficult to obtain using the pseudo-static analyses via the limit equilibrium method without conducting the numerical analyses [29–31]. Following the top-down procedure of Baker and Klein [13], Han and Leshchinsky [14] proposed a general analytical framework for the calculation of the tensile resistance distribution and the connection strength. Leshchinsky et al. [32,33] extrapolated the approach from a translational failure mechanism adopted by Han and Leshchinsky [14] to a rotational failure mechanism, which can uniformly solve the stability problem for both the reinforced wall and slope. However, their analyses are limited to the static condition. Compound failure is most likely due to failure of the GRS wall in the presence of seismicity [34].

In this study, the top-down procedure is extended into the seismic stability analysis of GRS walls. The distribution of the reinforcement load at a limit state is obtained for each layer, and then the required connection strength between the reinforcement and the facing is accordingly determined by the front-end pullout capacity. Using the reinforcement load distribution can preliminarily predict the seismic lateral displacement of the wall facing. Parametric studies are conducted to explore the effects of seismic forces on the stability and facing deformation of GRS walls.

2 Seismic analysis of GRS walls

2.1 Pseudo-static analysis based on limit equilibrium method

For the internal stability analysis of GRS walls under seismic conditions, the seismic active earth pressure based on the M–O method is used to determine the required tensile force of the reinforcement. To obtain the distribution of tensile load along with each reinforcement layer, the top-down procedure proposed by Han and Leshchinsky [14] is employed here incorporating the seismic force into the force balance of the wedged sliding mass, as shown in Fig. 1. Traditional pseudo-static analysis is conducted to investigate the seismic effects. To formulate the presented problem, the following assumptions are made.

1) The reinforced soil is homogeneous and cohesionless.

2) The Mohr–Coulomb (MC) failure criterion is used for the shear strength of cohesionless soil, and the strength is uniformly and completely mobilized in the whole of the reinforced soil.

3) The wall face is vertical and flexibly accords with the stacked facing units, e.g., concrete modular blocks and gabions. The potential downdrag force due to the facing units is ignored.

4) The toe resistance generated by the bottom leveling or the block pad is neglected.

5) The reinforced force at each reinforcement layer is horizontal and mobilized equally for a given sliding surface.

6) No surcharge is acting at the top of the wall.

7) The seismic loading is considered as the inertial force acting on the sliding mass using the horizontal or vertical seismic coefficient k_h, k_v.

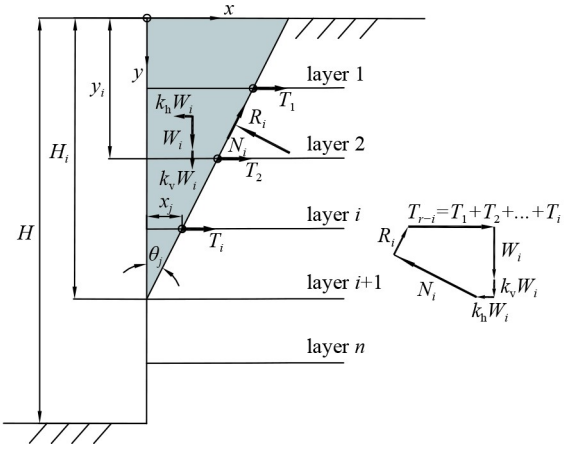

Fig. 1 Planar failure surface of GRS wall and force polygon.

As shown in Fig. 1, a planar slip surface with an inclined angle θ_j from the vertical wall face is emerging at the front point of the lower layer of the ith reinforcement. For the sliding body at a limit state, i.e., a factor of safety (FS) of 1.0, the acting forces include the vertical force because of the self-weight of the sliding mass W_i, which can be calculated as $0.5\gamma H_i^2 \tan\theta_j$ (γ = unit weight of reinforced soil, H_i = height of the emerging point of the slip surface from the wall top), the horizontal and vertical seismic loadings, the shear and normal forces (R_i and N_i) along the sliding surface, and the total reinforcement force T_{r-i}. Based on the vector polygon of these forces, the force balance of the sliding mass can be established in the sliding direction and its normal direction, as

$$R_i + R_c \sin\theta_j T_{r-i} = k_h W_i \sin\theta_j + (1+k_v) W_i \cos\theta_j, \quad (1)$$

$$N_i + k_h W_i \cos\theta_j = R_c \cos\theta_j T_{r-i} + (1+k_v) W_i \sin\theta_j, \quad (2)$$

where R_c is the coverage ratio of geosynthetic reinforcement, k_h and k_v are the horizontal and vertical seismic coefficients, respectively. Following the MC criterion, the shear force is equal to $N_i \tan\phi$ (ϕ is the internal friction angle of reinforced soil). Combining Eqs. (1) and (2) can obtain the total reinforcement load for the given planar slip surface, as

$$T_{r-i} = \frac{1}{2}\gamma H_i^2 \tan\theta_j \left(\frac{k_h}{R_c} + \frac{1+k_v}{R_c} \frac{\cos\theta_j - \sin\theta_j \tan\phi}{\sin\theta_j + \cos\theta_j \tan\phi} \right), \quad (3)$$

and it should be noted that the required reinforcement force T_{r-i} is the sum of the reinforcement intersecting with the slip surface. For the greater angle θ_j, the planar surface could not pass through the reinforcement at the upper layer. Such a compound failure is also involved in the determination of reinforcement load distribution.

2.2 Tensile force distribution and connection strength along each reinforcement layer

To determine the required tensile load distribution along each reinforcement layer, each reinforcement is divided into m small segments, and then the location of the segment x_j is expressed as

$$x_j = \Delta L(j - 0.5), \quad (4)$$

where x_j is the horizontal distance of the intersection of the slip surface with angle θ_j on the ith reinforcement determined tensile load T_i from the wall face and L is the length of reinforcement, $\Delta L = L/m$; $j = 1,\ldots,m$. Then, the angle θ_j can be obtained from the geometrical and trigonometric relations, as

$$\tan\theta_j = \frac{x_j}{H_i - y_i}, \quad (5)$$

where y_i is the vertical distance of the ith reinforcement from the wall crest. Substituting the obtained angle into Eq. (3) and then dividing by the number of the slip surface intersected reinforcements can calculate the average tensile force of the intersected reinforcements. Based on the top-down procedure, the calculation of the reinforcement load distribution begins at the top layer and then repeated layer by layer. It should be noted that the initial tensile force for all the segments is assigned to be zero. After obtaining the tensile force of the ith layer at the location of the intersection with a given planar surface, the force needs to be updated at the upper layered reinforcements via comparison with previous results, i.e., by selecting the greater force, but while maintaining the total reinforcement forces in limit equilibrium.

The maximum value of the required tensile force, T_{max}, should be less than the allowable long-term strength of the reinforcement, T_{al}, which is the ultimate strength, T_{ult}, divided by the reduction factors for install damage, durability, and creep. Otherwise, the reinforcement should be lengthened or selected with higher ultimate strength. Additionally, the required tensile force is also limited by the pullout resistance, as shown in Fig. 2. The available pullout resistance at the rear and front of the ith reinforcement layer, respectively referred to as $T_{po(r)-i}$ and $T_{po(f)-i}$, can be calculated as

$$T_{po(r)-i} = 2\left(L - x_j\right)\gamma y_i C_i R_c \tan\phi, \quad (6a)$$

$$T_{po(f)-i} = 2x_j \gamma y_i C_i R_c \tan\phi, \quad (6b)$$

where C_i is the interaction coefficient between the reinforcement layer and the reinforced soil, here selecting $C_i = 0.8$ for geogrid reinforcement. Note that the available rear pullout resistance is zero for $x_j = L$. The calculated reinforcement load distribution cannot exceed the envelope of the pullout resistance. Ideally, the tensile force curve is tangential to the available resistance line at the rear or front reinforcement. Otherwise, the tensile force of the rear reinforcement will be constrained and the corresponding insufficient force is compensated for by the lower layered reinforcements. For the front reinforcement, the facing can provide additional resistance to pullout because of the interaction of the

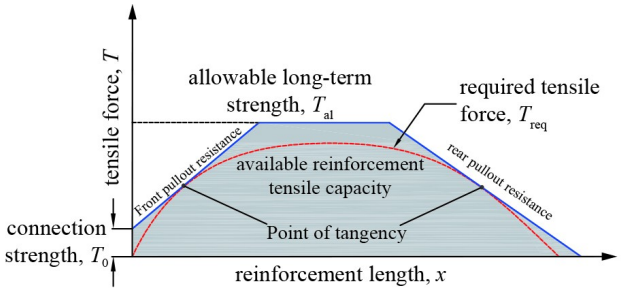

Fig. 2 Required tensile force and connection strength determined by front and rear pullout resistance.

reinforcement with the soil. To make the required tensile force curve tangential to the available front pullout resistance line, an adequate connection strength at the facing should be imposed, and then the available front pullout resistance can be expressed as

$$T_{\mathrm{po(f)}-i} = T_{\mathrm{o}-i} + 2x_j\gamma y_i C_{\mathrm{i}} R_{\mathrm{c}} \tan\phi, \tag{7}$$

where $T_{\mathrm{o}-i}$ is the adequate connection strength between the ith reinforcement and wall facing. The connection strength can physically develop because of the anchorage of the reinforcement between stacked concrete modular blocks or because of a mechanical connection to the facing. Combining with the constraints of the available front and rear pullout resistances, the reinforcement load distribution is readjusted for each layer, and the corresponding connection strength is determined at the limit state of the seismic GRS wall.

To implement the developed top-down procedure, generic steps are illustrated in Fig. 3. The procedure is characterized by the layer-by-layer analysis of each potential slip surface. Carrying out the iterative process can obtain the distribution of the tensile load along each reinforcement and can determine T_{o} and $T_{\max}$ for each layer.

2.3 Estimation of seismic lateral deformation

GRS walls have the great advantage of flexibility because of their extensible reinforcement and can tolerate lateral movement, especially during earthquakes. As investigated by Allen and Bathurst [1], the GRS walls exhibit good performance for total reinforcement strains less than 3% (the ultimate strain of geosynthetics is about 15%). The seismic effects can increase the tensile force along the reinforcement and then yield to a lateral facing displacement response. An approximate method is used here to estimate the horizontal displacement of the GRS wall and then to demonstrate the seismic effects on the facing deformation profile. Note that the estimative results according to this method correspond to peak lateral deformations and neglect deformation because of the sliding of the reinforced soil zone.

For each reinforcement segment, its strain can be calculated using the obtained tensile force divided by the reinforcement stiffness. The sum of the reinforcement strain is regarded as the horizontal facing displacement at the limit state, expressed as

$$d_i = L\sum_{j=1}^{m}\left(\frac{T_i\left(x_j\right)}{J}\right), \tag{8}$$

where d_i is the lateral facing distance at the location of the ith layer; $T_i(x_j)$ is the required tensile load of the segmental reinforcement with the location x_j; and J is the average stiffness of reinforcement, assuming the constant stiffness in this estimation and selecting J = 500 kN/m here for geogrid reinforcement. Such an approximation ignores the seismic response of GRS walls and earthquake time history. Once the distribution of the tensile load along the reinforcement is determined via the top-down procedure, using Eq. (8) can preliminarily estimate the lateral facing displacement of a GRS wall.

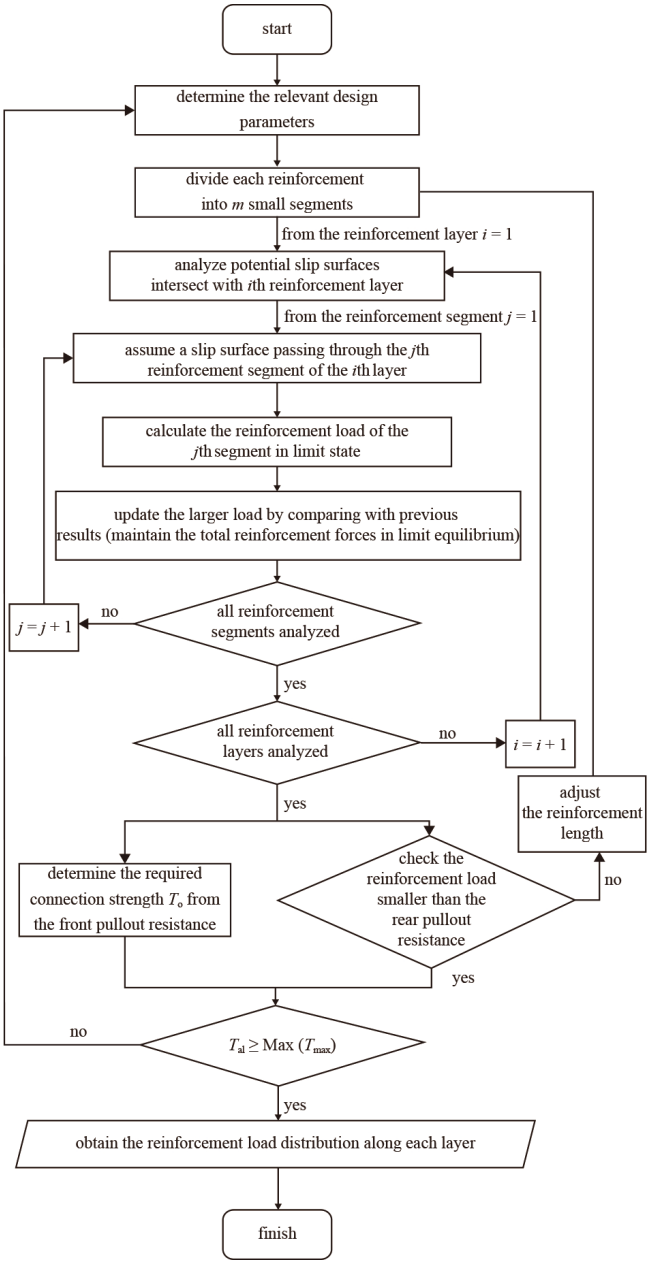

Fig. 3 Flow chart for the numerical calculations of top-down procedure.

2.4 Verification of calculated results

Following the top-down procedure, the distribution of the tensile load along each reinforcement can be calculated

and then compared with the static results of Han and Leshchinsky [14] for the validation of the extended method, as shown in Fig. 4(a). A baseline case considered by Han and Leshchinsky [14] is revisited here, and its parameters include wall height H = 3 m, reinforcement space S_v = 0.6 m, backfill unit weight γ = 20 kN/m^3, friction angle ϕ = 30°, reinforcement length L = 3 m, interaction coefficient C_i = 0.8, and coverage ratio R_c = 50%. The obtained results for each reinforcement are in good agreement with those presented by Han and Leshchinsky [14]. The ratio of the connection strength and maximum tensile force is determined for R_c = 50% and 100% of the baseline case, as illustrated in Fig. 4(b). The comparisons indicate the accuracy of the presented method for a static condition. The static solutions can be also compared with the experimental results of the centrifuge test given by Mohamed et al. [27,35]. The parameters of the centrifuge model include vertical wall height H = 340 mm, reinforcement space S_v = 20 mm, backfill unit weight γ = 15 kN/m^3, friction angle ϕ = 39.5°, reinforcement length L = 224 mm, and coverage ratio R_c = 100%. The failure g-level of the centrifuge model reaches 16, and then the corresponding situation can be regarded as the limit state. Figure 5(a) compares the critical failure surface obtained from the centrifuge test [27] and those predicted by the top-down procedure. The predicted failure surface is closer to the failure surface of the test. The surface of the test is shallower than the predicted surface and does not pass through the wall toe: This may be attributed to the constraint of the firm foundation in the model test. Figure 5(b) compares the mobilized tensile load distributions obtained from the FE method [35] and the presented method. It can be found that the calculated maximum tensile forces (black circulars in Fig. 5(b), T_{max} = 0.14 kN/m) are slightly larger than the experimental results (blue squares in Fig. 5(b), T_{max} = 0.12 kN/m). The toe resistance and friction between stacked facias in the FE analyses could yield a smaller reinforcement load. The presented method neglected their influences, as shown in the assumptions.

As presented in the seismic design method of NCMA [12], the seismic active earth pressure based on the M–O method is used to determine the required tensile force for internal stability of seismic GRS wall. The sum of the required reinforcement tensions can be expressed as

$$\sum_{i=1}^{n} T_{max-i} = \frac{1}{2}\gamma H^2 (1+k_v) K_{AE}, \tag{9}$$

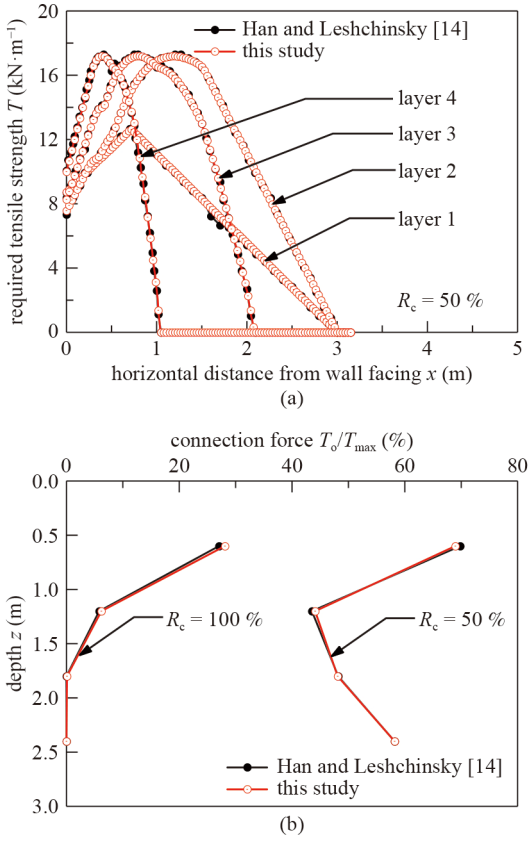

Fig. 4 Verification of calculated results for the baseline case given by Han and Leshchinsky [14]. (a) x–T; (b) T_o/T_{max}–z.

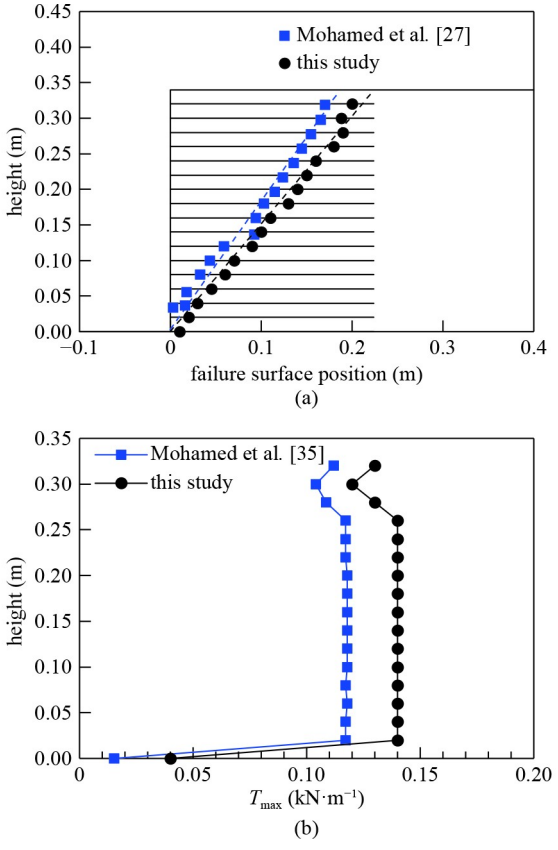

Fig. 5 Verification of calculated results for the static case given by Mohamed et al. [27,35]. (a) Failure surface position vs. height; (b) T_{max} vs. height.

where K_{AE} is the dynamic earth pressure coefficient and can be calculated from the M–O method as

$$K_{AE}=\frac{\cos^2(\phi-\alpha)}{\cos^2\alpha\left(1+\sqrt{\frac{\sin\phi\sin(\phi-\alpha)}{\cos\alpha}}\right)^2}, \tag{10}$$

where angle α is the seismic inertia angle and is expressed as follows

$$\alpha=\tan^{-1}\left(\frac{k_h}{1+k_v}\right). \tag{11}$$

The inclined angle of the critical planar surface for seismic internal stability can be determined as

$$\theta_{cr}=\cot^{-1}\left(\frac{\cos\phi}{\sqrt{\frac{1}{1-\cot\phi\tan\alpha}}-\sin\phi}\right). \tag{12}$$

Using Eq. (10) in the baseline case above can obtain the values for K_{AE} for the horizontal seismic acceleration k_h = 0.1, 0.2, and 0.3, as shown in Table 1. The vertical acceleration is ignored here. To compare with the M–O method, the results calculated from this study are presented in the form of $K_a = \sum T_{max}/(0.5\gamma H^2)$. A long reinforcement with length L = 6 m is also considered, and the corresponding results are identical to the M–O solutions. However, for L = 3 m, the coefficient K_a is larger than the M–O solution, except for the static condition. Figure 6 illustrates the locations of T_{max} for each reinforcement layer using the presented method. For the case with long reinforcement, the trace of the locations is a plane, of which the inclined angle from the vertical wall is consistent with the critical angle θ_{cr} determined via the M–O method (i.e., Eq. (12)). For L = 3 m, the T_{max} trace of the seismic GRS wall is not a plane. The locations of T_{max} for the middle and lower layers approach the end of the reinforcements because of the greater T_{max} required for the compound failure mechanism.

Liu [36] conducted nonlinear dynamic FE analyses of a seismic GRS wall and obtained the distributions of the maximum reinforcement load along the wall height. The numerical model is considered here for the comparison of the seismic condition, and the parameters are given: wall height H = 6 m, reinforcement space S_v = 0.6 m, backfill unit weight γ = 16 kN/m^3, friction angle ϕ = 40°, reinforcement length $L = 0.7H$ = 4.2 m, coverage ratio R_c = 100%. Different earthquake excitations (EI-Centro, Taft, and Kobe) were used by Liu [36], and the obtained values of T_{max} for each layer are compared with the results calculated by the presented method (shown in Fig. 7). They are slightly greater than the numerical results, but their distribution is similar. The differences of the maximum tensile forces can be attributed to the earthquake time history ignored in the pseudo-static analyses, which yield a conservative evaluation of seismic stability of GRS walls.

3 Parametric study

The presented method is used in a baseline case of a GRS wall with H = 6 m, S_v = 0.6 m, $L = 0.7H$ = 4.2 m, R_c = 100%, γ = 20 kN/m^3, and ϕ = 30°. The seismic cases with the acceleration coefficient k_h = 0.1, 0.2, and 0.3 are considered, and the static case (k_h = 0.0) is also included to demonstrate the seismic effects through comparisons. Conducting a parametric study can lead to the exploration of their influences on the seismic behavior of the GRS wall at a limit state. These parameters include backfill friction angle, reinforcement length, vertical seismic acceleration, and secondary reinforcement.

3.1 Influence of the backfill friction angle

The quality of the reinforced fill is very important for the safety design of a GRS wall. As guided by FHWA [11], the frictional angle of the granular fill should be greater than 30°, but less than 40° for GRS wall design. In practice, low-quality backfills with ϕ < 30° may also be used. Here, different frictional angles of the backfill ϕ = 25°, 30°, 35°, and 40° are considered in the baseline case. Figure 8 shows the obtained values of T_{max} and T_o for each reinforcement layer of the seismic GRS wall at a limit state. Expectedly, the required T_{max} and T_o increase with the decreasing frictional angle of the backfill. The connection strength is much smaller than the value of T_{max} required in the upper layers. As the magnitude of the

Table 1 Comparisons of the coefficients of seismic active earth pressure between this study and the M–O method

k_h	L = 3 m		L = 6 m		K_{AE}
	$\sum T_{max}$ (kPa)	K_a	$\sum T_{max}$ (kPa)	K_a	
0.0	30.00	0.3333	30.00	0.3333	0.3333
0.1	37.31	0.4145	35.69	0.3966	0.3966
0.2	56.38	0.6265	42.59	0.4733	0.4733
0.3	88.19	0.9799	51.24	0.5693	0.5693

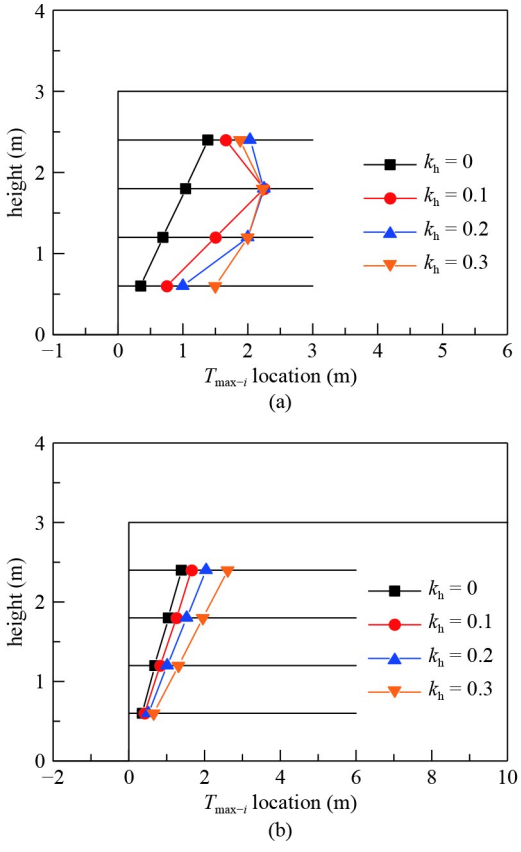

Fig. 6 Location of T_{max} for each reinforcement layer of the baseline case $R_c = 100\%$: (a) $L = 3$ m; (b) $L = 6$ m.

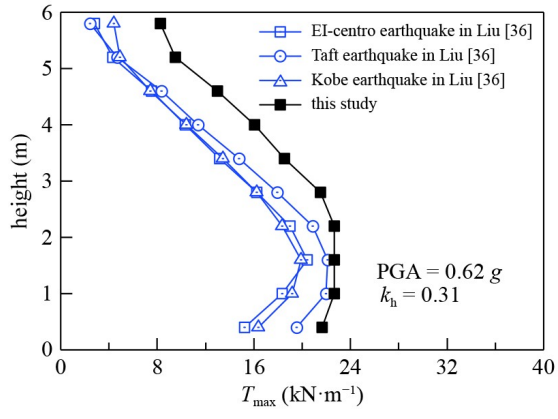

Fig. 7 Verification of calculated results for the seismic case given by Liu [36].

horizontal seismicity increases, T_{max} greatly increases, especially for the lower layers. Figure 9 gives the locus of T_{max} for each layer. It can be seen that their locations grow farther from the wall facing as the acceleration coefficient k_h increases. The planar trace for the T_{max} location in the lower layer becomes shallower with the frictional angle. The T_{max} locations of the upper layers approach the end of the reinforcement and are closer as ϕ

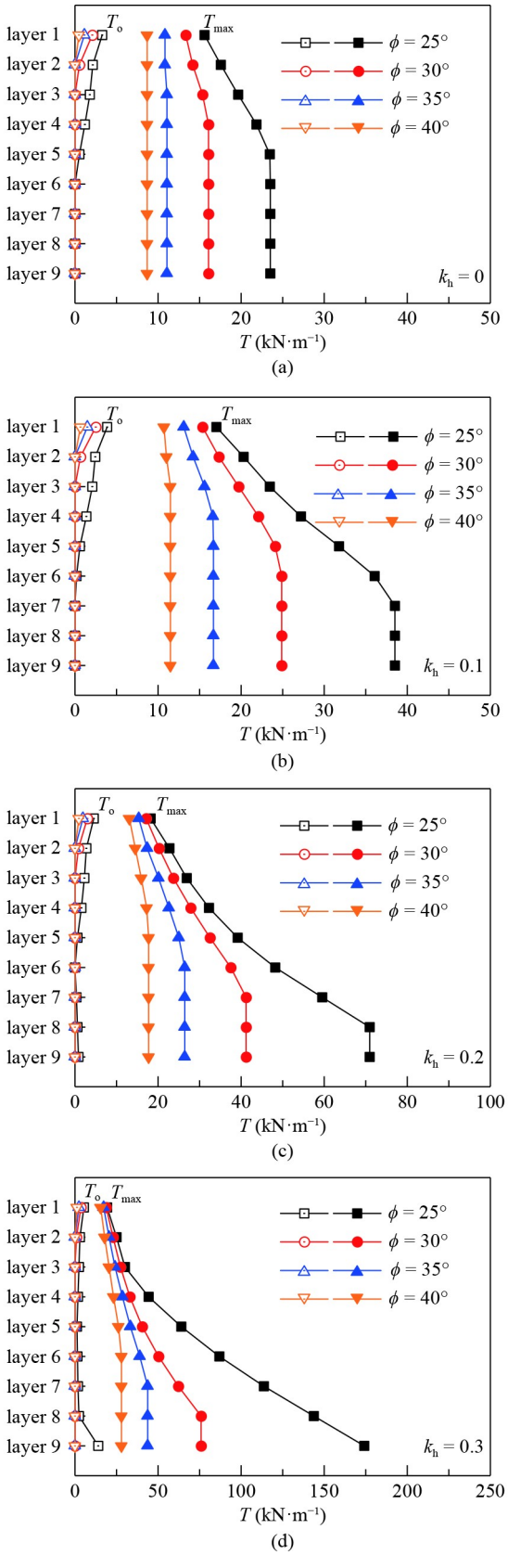

Fig. 8 Effect of backfill friction angle on required strength T_{max} and T_o for each reinforcement layer. (a) $k_h = 0$; (b) $k_h = 0.1$; (c) $k_h = 0.2$; (d) $k_h = 0.3$.

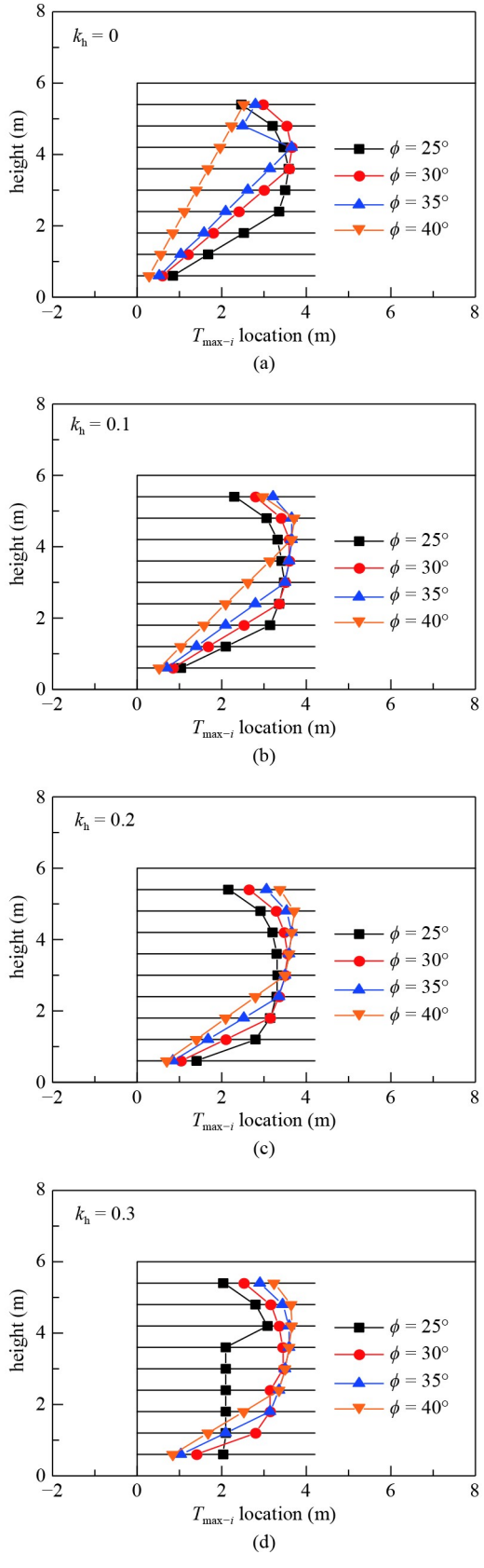

Fig. 9 Effect of backfill friction angle on the location of T_{max} for each reinforcement layer. (a) $k_h = 0$; (b) $k_h = 0.1$; (c) $k_h = 0.2$; (d) $k_h = 0.3$.

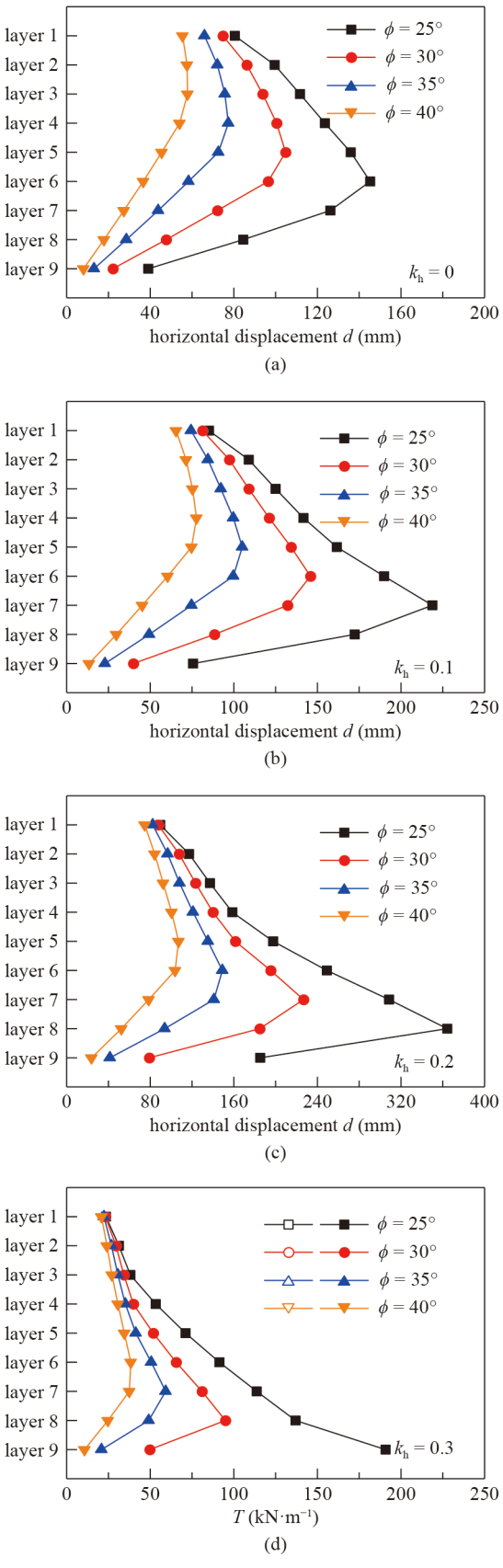

Fig. 10 Effect of backfill friction angle on predicted lateral displacement. (a) $k_h = 0$; (b) $k_h = 0.1$; (c) $k_h = 0.2$; (d) $k_h = 0.3$.

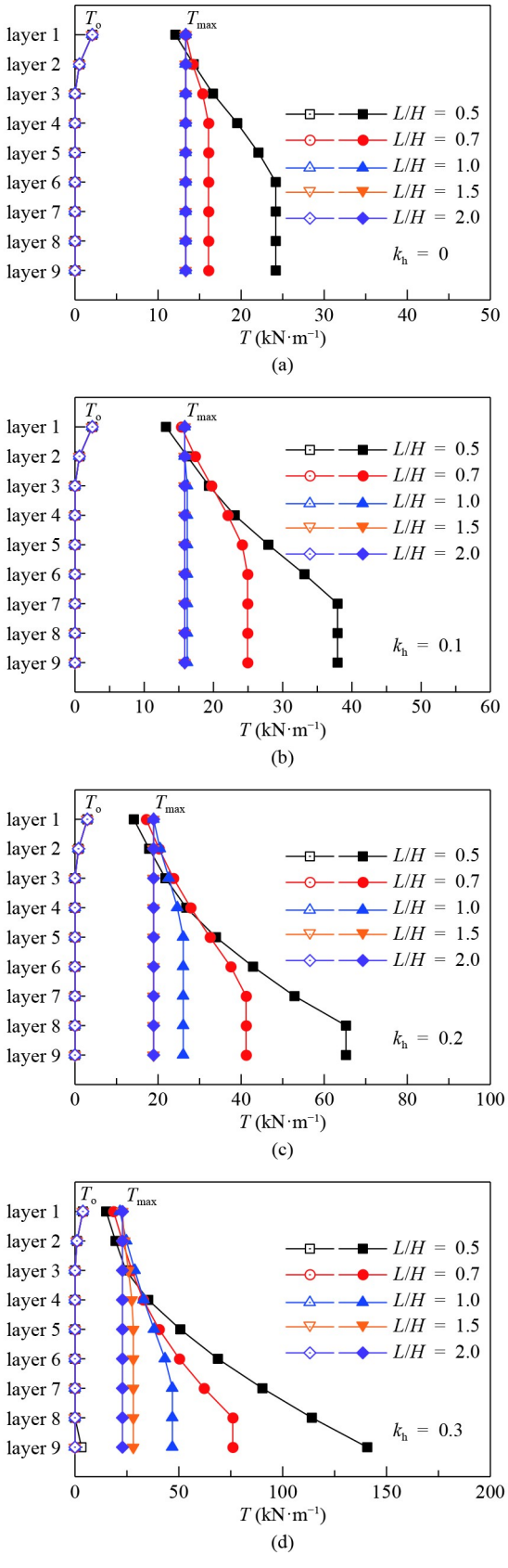

Fig. 11 Effect of reinforcement length on required strength T_{max} and T_o for each reinforcement layer. (a) k_h = 0; (b) k_h = 0.1; (c) k_h = 0.2; (d) k_h = 0.3.

increases.

Using the approximate method based on Eq. (8), the lateral facing displacement of the GRS wall can be assessed, as shown in Fig. 10. Expectedly, the displacement becomes larger with increasing k_h and decreasing ϕ. From the outward deformation profile of the facing, excessive displacement occurs in the local portion and yields to wall-facing bulging. As k_h increases and ϕ decreases, the location of the maximum displacement moves from the middle to the lower portions. The use of good quality fill with a great friction angle ($\phi \geqslant 30°$) could decrease the maximum displacement by 50% compared with that for selecting low-quality fill, especially for strong earthquakes.

3.2 Influence of reinforcement length

Different values of reinforcement length L/H = 0.5, 0.7, 1.0, 1.5, and 2.0 are considered, and Fig. 11 presents the calculated T_{max} and T_o. The reinforcement length has effects on T_{max} but has no effects on T_o. For the static condition, the increase of the reinforcement length has no influence on T_{max} for L more than 0.7H required by AASHTO [10]. However, as the seismic coefficient k_h increases, more pullout resistances are provided in the lower layers and result in larger T_{max}, which needs to be provided by geosynthetic reinforcement with greater T_{ult}. Figure 12 shows the influences of the reinforcement length on the locations of T_{max} for each layer. For longer reinforcement length, the trace of T_{max} coincides with the planar surface obtained from the M–O method. Once the length is insufficient, the locus of T_{max} moves toward the end of the reinforcement. For short reinforcement, the compound failure surface results in a greater tension load on the lower layer. As presented in AASHTO [10], because of the decrease in the required tensile force of the lower layer, the length of reinforcement in the upper two layers can exceed 0.7H to improve the seismic performance.

Figure 13 illustrates the profile of the lateral deformation of GRS walls with different reinforcement lengths. As the length increases, the location of the maximum displacement changes from the bottom to the top of the wall. However, the resulting maximum displacement increases slightly with the length. The reason for this may be attributed to the constant stiffness of the reinforcement considered in the estimation.

3.3 Influence of vertical seismic acceleration

Historical earthquake records, e.g., records about the Loma Prieta earthquake, the Northridge earthquake, and the Hanshin earthquake, have demonstrated the obvious vertical component of the earthquake acceleration, even more than twice of the horizontal acceleration, as

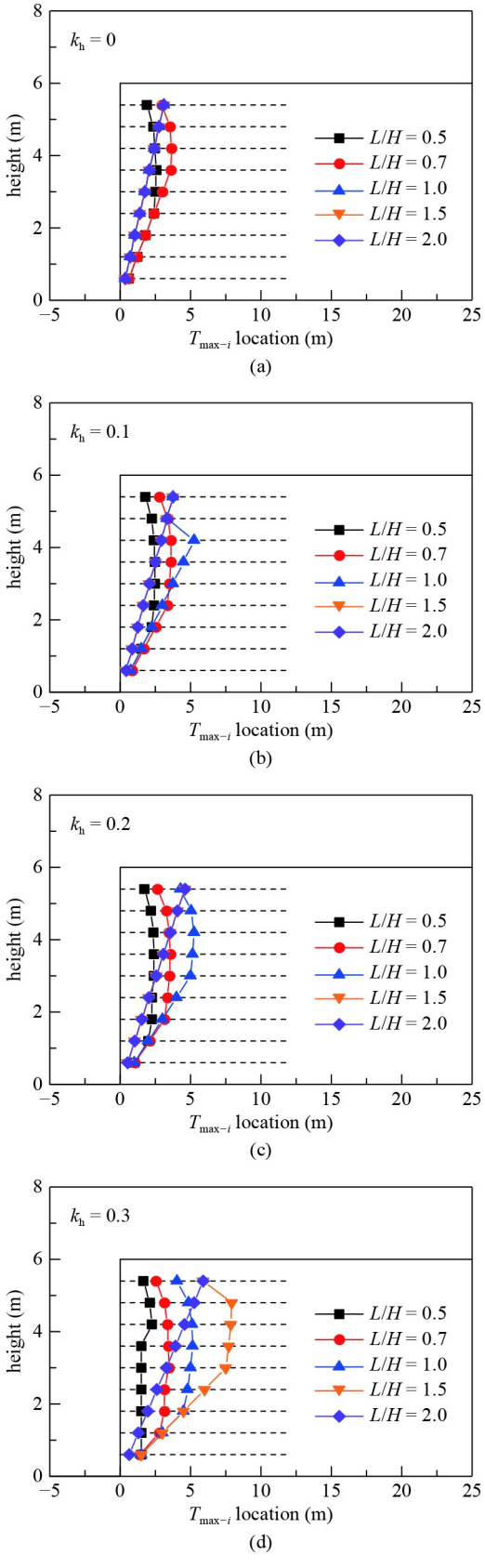

Fig. 12 Effect of reinforcement length on the location of T_{max} for each reinforcement layer. (a) $k_h = 0$; (b) $k_h = 0.1$; (c) $k_h = 0.2$; (d) $k_h = 0.3$.

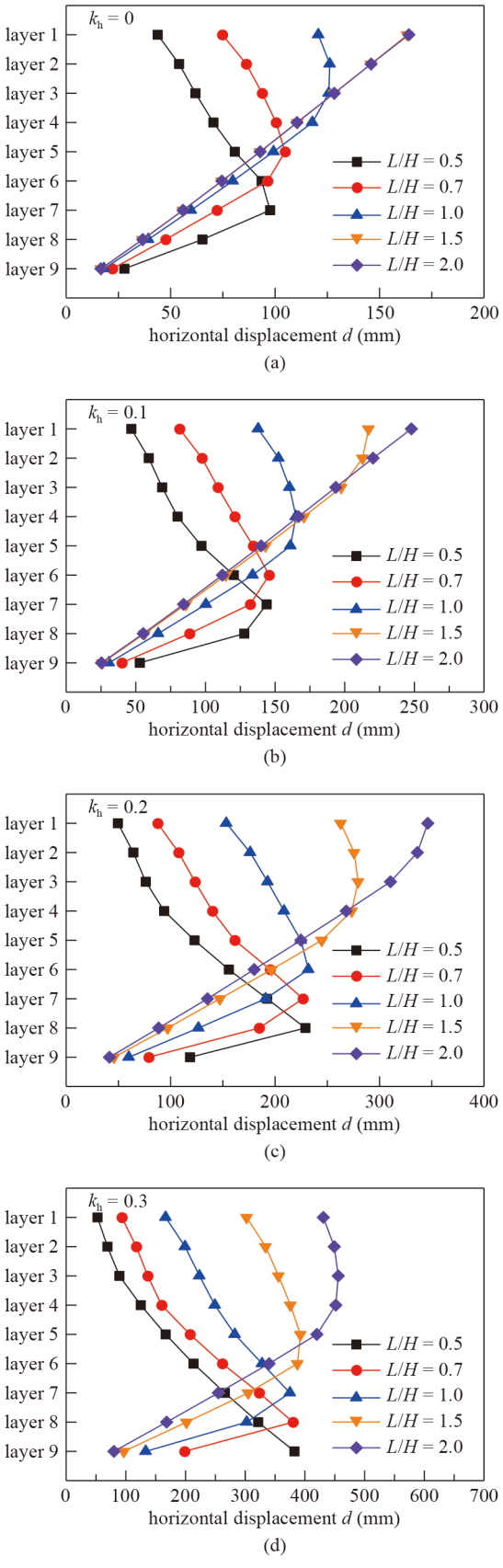

Fig. 13 Effect of reinforcement length on predicted lateral displacement. (a) $k_h = 0$; (b) $k_h = 0.1$; (c) $k_h = 0.2$; (d) $k_h = 0.3$.

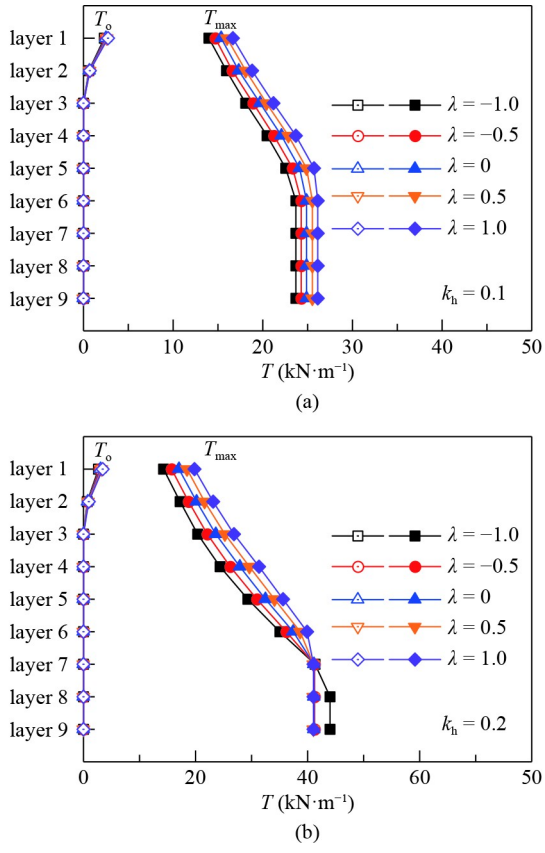

Fig. 14 Effect of vertical seismicity on required strength T_{max} and T_o for each reinforcement layer. (a) $k_h = 0.1$; (b) $k_h = 0.2$.

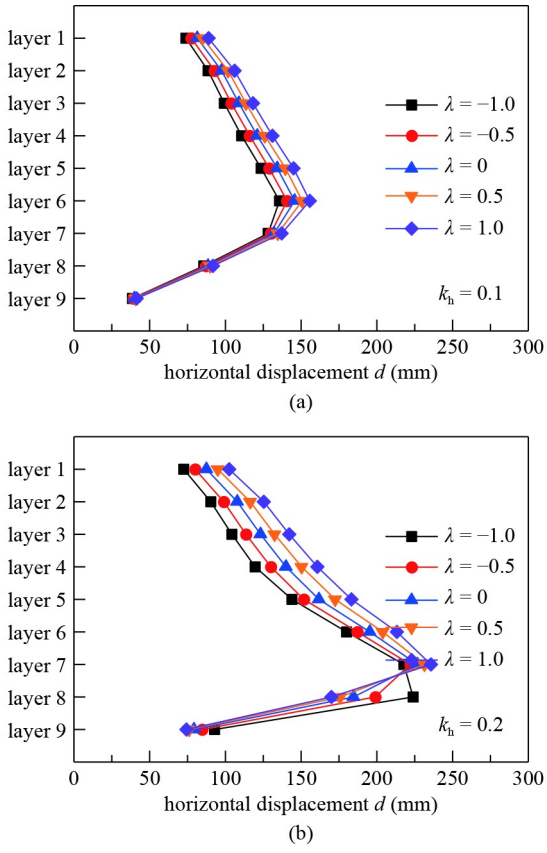

Fig. 15 Effect of vertical seismicity on predicted lateral displacement. (a) $k_h = 0.1$; (b) $k_h = 0.2$.

evidenced in the Iwate-Miyagi earthquake. Therefore, to investigate its influence on required reinforcement force and lateral deformation of GRS walls, the vertical seismic acceleration combining with the horizontal acceleration is considered here, as shown in Figs. 14 and 15. The parameter λ is the ratio of the vertical and horizontal acceleration coefficients, and the positive value represents the vertical acceleration acting downward. As shown in Fig. 14, the vertical acceleration has effects on the required T_{max} but has a negligent influence on the profile of T_{max} distribution. The downward action of the vertical acceleration yields greater T_{max}, which is in good agreement with that found by Ling and Leshchinsky [25]. Note that for $k_h = 0.2$, the values of T_{max} in the lower layers are the same, except for $\lambda = -1.0$. The k_v effects can be ignored on the connection strength. From the estimated horizontal displacements, the vertical acceleration has an insignificant effect on the displacement of the lower layer but has great effects on that of the upper layer.

3.4 Influence of secondary reinforcement

The layout of the secondary reinforcement is beneficial to the stability of a GRS wall and is often used in practical design, especially for seismic conditions. The influences of the secondary reinforcement are investigated in a seismic GRS wall with $H = 3$ and 9 m. Figure 16 illustrates the required T_{max} of the primary and secondary reinforcements in a 3-m-high wall. The results of T_{max} without the secondary reinforcement are also included. From the comparisons, the secondary reinforcement not only largely reduces the required T_{max} but also nearly results in zero connection strength. Typically, the length $L_s = 1$ m can decrease the required T_{max} of the primary reinforcement to half. The length of the secondary reinforcement has minor effects on its tensile force. From the estimated lateral displacement shown in Fig. 17, short secondary reinforcement can significantly decrease the facing displacement. The resulted deformation reduces with the length L_s, at least 50% for $L_s = 1$ m.

For a 9-m-high wall, the required T_{max} of the primary and secondary reinforcements and the connection strength T_o are obtained, as shown in Fig. 18. The secondary reinforcement still can reduce the values of T_{max} and T_o for each primary layer in most cases. It should be noted that, when $k_h = 0.3$, shorter secondary reinforcement can yield greater connection strength in the lower layers. Figure 19 shows the influences of the secondary

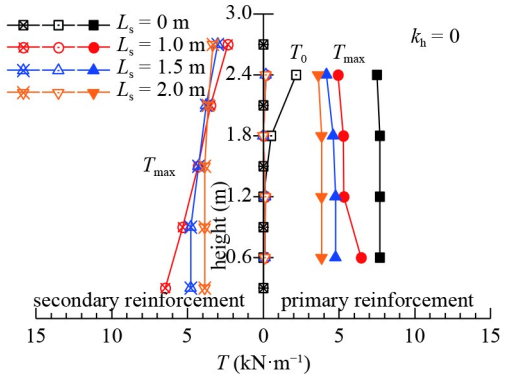

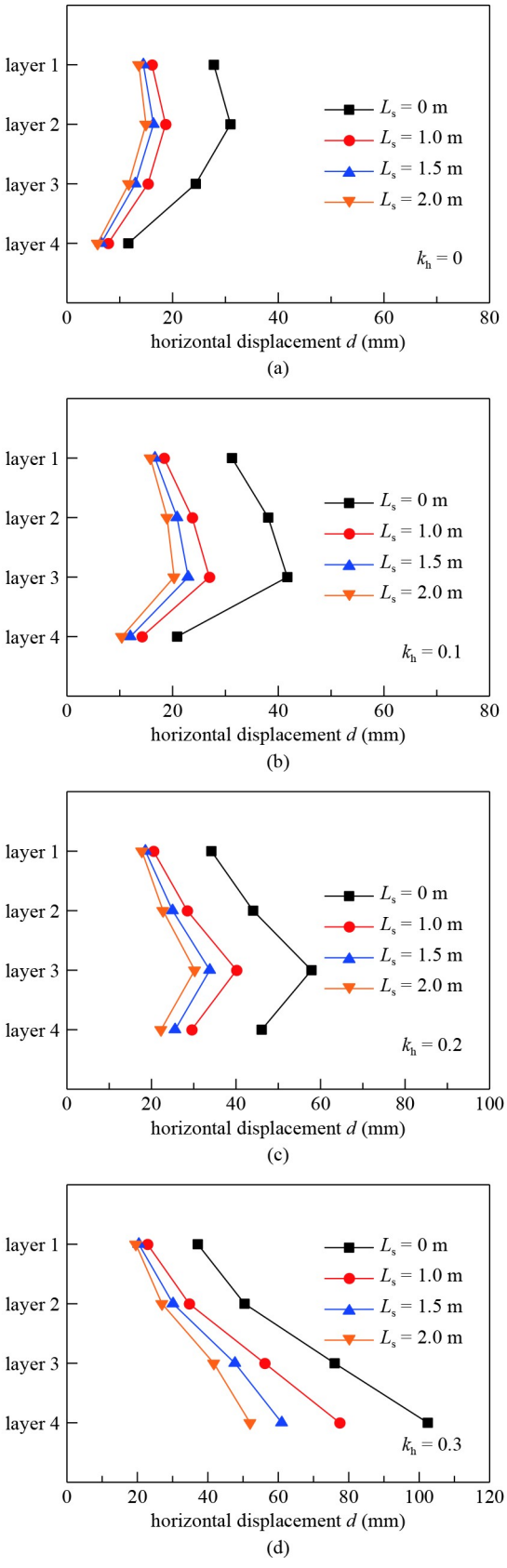

Fig. 16 Effect of secondary reinforcement on required strength T_{max} and T_o for each reinforcement layer (H = 3 m). (a) k_h = 0; (b) k_h = 0.1; (c) k_h = 0.2; (d) k_h = 0.3.

Fig. 17 Effect of secondary reinforcement on predicted lateral displacement (H = 3 m). (a) k_h = 0; (b) k_h = 0.1; (c) k_h = 0.2; (d) k_h = 0.3.

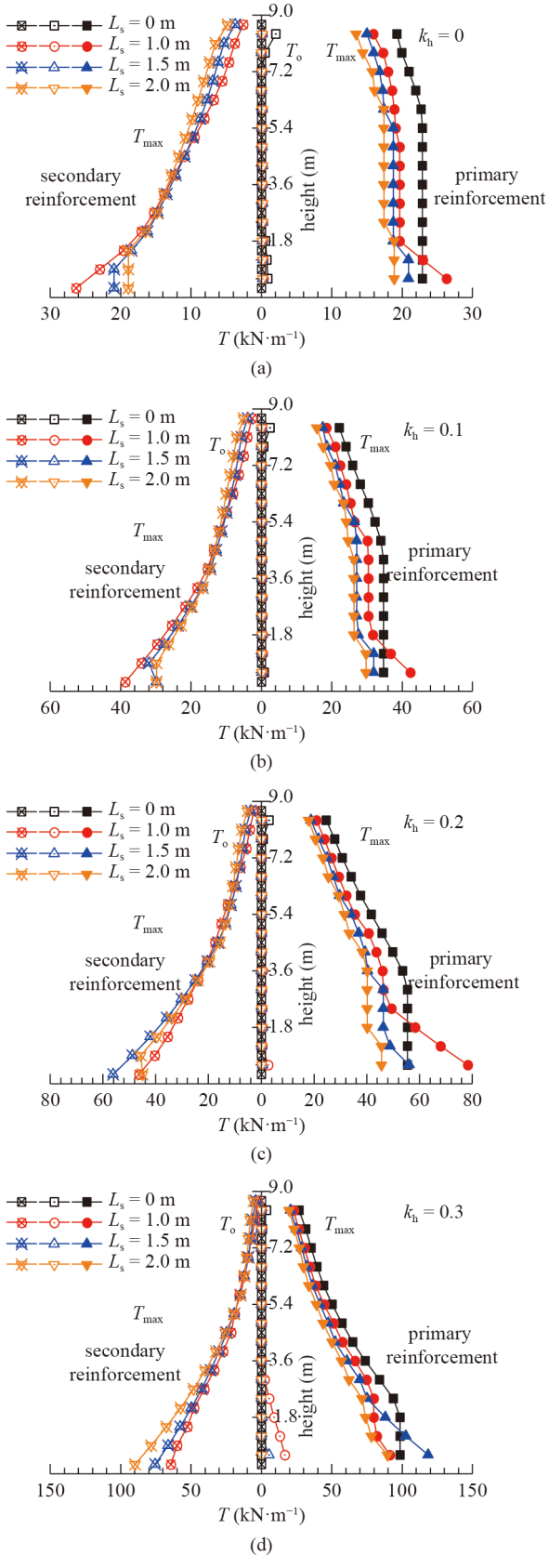

Fig. 18 Effect of secondary reinforcement on required strength T_{max} and T_o for each reinforcement layer (H = 9 m). (a) k_h = 0; (b) k_h = 0.1; (c) k_h = 0.2; (d) k_h = 0.3.

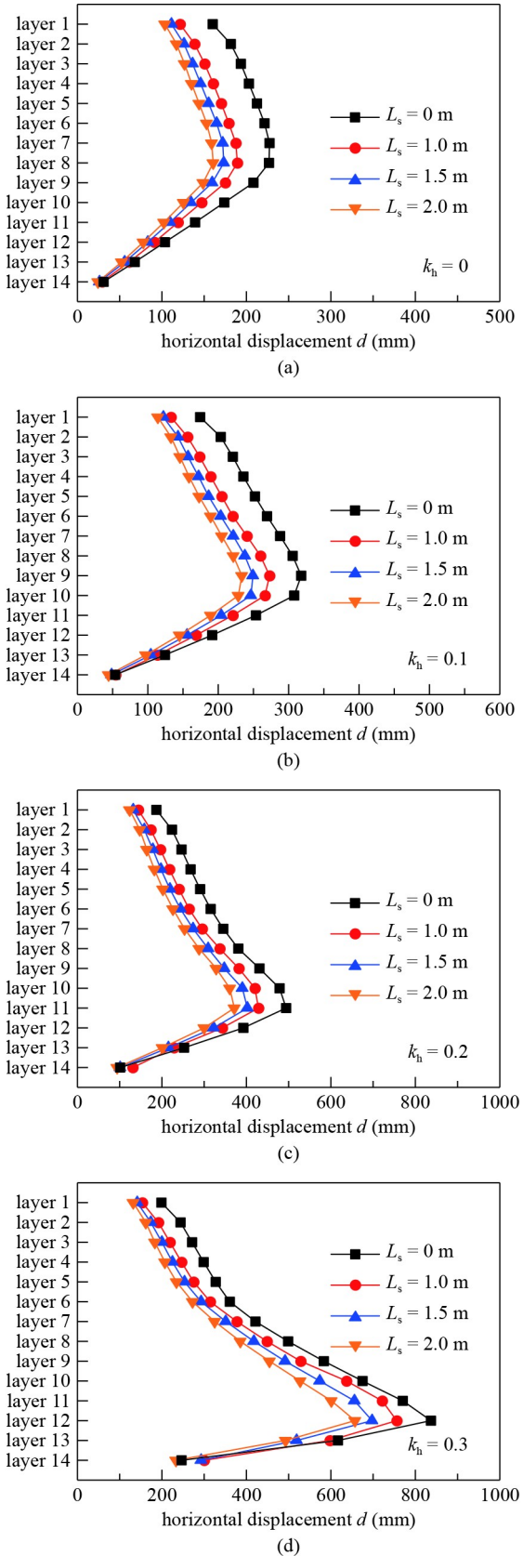

Fig. 19 Effect of secondary reinforcement on predicted lateral displacement (H = 9 m). (a) k_h = 0; (b) k_h = 0.1; (c) k_h = 0.2; (d) k_h = 0.3.

reinforcement on the lateral deformation of the wall. The profile of the facing deformation is not changed by the secondary reinforcement, but it largely reduces the horizontal displacements, especially for the upper and middle layers.

4 Conclusions

This study extended the top-down procedure to calculate the reinforcement load distribution of GRS walls from the static condition to the seismic condition. Using the front-end pullout capacity for each reinforcement layer determines the required connection strength between the reinforcement and the facing. An approximate approach to estimate the lateral displacement of the seismic GRS wall is presented based on the stability analyses. A parametric study is conducted to investigate the seismic effects on the stability and lateral deformation of GRS walls. Some conclusions can be drawn below.

1) When the reinforcement is long enough for seismic stability of the GRS wall, its maximum tensile force obtained from the presented analyses is identical to the active earth pressure based on the M–O method. The insufficient reinforcements of seismic GRS walls can lead to compound failures and then make greater tensile force required in the lower layers.

2) The decrease of the backfill friction angle can significantly increase the required tensile force, connection strength, and lateral facing deformation of a seismic GRS wall, especially for the lower layers. The use of low-quality backfill must be paid more attention to the seismic design of the GRS wall.

3) Using short reinforcements in seismic design could largely increase the required tensile force in the mid and lower layers of the GRS wall. The influences of the reinforcement length on the required connection strength are insignificant and can be neglected in design.

4) The vertical seismic acceleration acting downward results in a slight increase of the reinforcement tensile force and horizontal displacement in the upper layer of the GRS wall. More attention should be paid to strengthening the connection strength between the reinforcements and facing units of the GRS wall, especially in the upper layer.

5) The short secondary reinforcement can largely reduce the tensions of the primary reinforcement and the lateral displacement of facing. Using the secondary reinforcement is good for the seismic stability of the GRS wall.

The presented results are limited to the tensile force of the GRS wall at a limit state of $FS = 1.0$ (i.e., the strength of backfill is fully mobilized). Using the strength reduction method can obtain the distribution of reinforcement tension for a prescribed FS. Once the calculated results are consistent with the measured reinforcement loads, the corresponding FS can be used in the stability assessment of the GRS wall. Furthermore, the analytical method can be expanded to include the tension cracks [37], surcharge loads [38,39], and permanent displacements [40,41]. The stability analyses of seismic GRS walls based on top-down procedure take different possible failure surfaces into account and can be further verified using numerical methods (i.e., the phase field model [42–44]).

Acknowledgements This study was supported by the National Natural Science Foundation of China (Grant Nos. 52078185, 51878248, and 41630638).

References

1. Allen T M, Bathurst R J. Observed long-term performance of geosynthetic walls and implications for design. Geosynthetics International, 2002, 9(5–6): 567−606
2. Allen T M, Bathurst R J. Performance of an 11 m high block-faced geogrid wall designed using the K-stiffness method. Canadian Geotechnical Journal, 2014, 51(1): 16−29
3. Stuedlein A W, Bailey M, Lindquist D, Sankey J, Neely W J. Design and performance of a 46-m-high MSE wall. Journal of Geotechnical and Geoenvironmental Engineering, 2010, 136(6): 786−796
4. Jiang Y, Han J, Parsons R L, Brennan J J. Field instrumentation and evaluation of modular-block MSE walls with secondary geogrid layers. Journal of Geotechnical and Geoenvironmental Engineering, 2016, 142(12): 05016002
5. Salem M A, Hammad M A, Amer M I. Field monitoring and numerical modeling of 4.4 m-high mechanically stabilized earth wall. Geosynthetics International, 2018, 25(5): 545−559
6. Shishegaran A, Khalili M R, Karami B, Rabczuk T, Shishegaran A. Computational predictions for estimating the maximum deflection of reinforced concrete panels subjected to the blast load. International Journal of Impact Engineering, 2020, 139: 103527
7. Shishegaran A, Ghasemi M R, Varaee H. Performance of a novel bent-up bars system not interacting with concrete. Frontiers of Structural and Civil Engineering, 2019, 13(6): 1301−1315
8. Tatsuoka F, Tateyama M, Mohri Y, Matsushima K. Remedial treatment of soil structures using geosynthetic-reinforcing technology. Geotextiles and Geomembranes, 2007, 25(4–5): 204−220
9. Ling H I, Leshchinsky D, Chou N N S. Post-earthquake investigation on several geosynthetic-reinforced soil retaining walls and slopes during the Ji-Ji earthquake of Taiwan (China). Soil Dynamics and Earthquake Engineering, 2001, 21(4): 297−313
10. Steudle K T, Horsley J. AASHTO LRFD Bridge Design Specifications. 6th ed. Washington, D.C.: American Association of State Highway and Transportation Officials, 2012
11. Berg R R, Christopher B R, Samtani N C. Mechanically Stabilized Earth Walls and Reinforced Soil Slopes Design and Construction Guidelines. Washington, D.C.: Federal Highway Administration, 2009

12. Collin J G. Design Manual for Segmental Retaining Walls. 3rd ed. Herndon, VA: National Concrete Masonry Association, 2009
13. Baker R, Klein Y. An integrated limiting equilibrium approach for design of reinforced soil retaining structures: Part I—formulation. Geotextiles and Geomembranes, 2004, 22(3): 119−150
14. Han J, Leshchinsky D. General analytical framework for design of flexible reinforced earth structures. Journal of Geotechnical and Geoenvironmental Engineering, 2006, 132(11): 1427−1435
15. Leshchinsky D, Zhu F, Meehan C L. Required unfactored strength of geosynthetic in reinforced earth structures. Journal of Geotechnical and Geoenvironmental Engineering, 2010, 136(2): 281−289
16. Ehrlich M, Mitchell J K. Working stress design method for reinforced soil walls. Journal of Geotechnical Engineering, 1994, 120(4): 625−645
17. Liu H, Won M S. Stress dilatancy and reinforcement load of vertical-reinforced soil composite: analytical method. Journal of Engineering Mechanics, 2014, 140(3): 630−639
18. Ehrlich M, Mirmoradi S H. A simplified working stress design method for reinforced soil walls. Geotechnique, 2016, 66(10): 854−863
19. Allen T M, Bathurst R J, Holtz R D, Walters D, Lee W F. A new working stress method for prediction of reinforcement loads in geosynthetic walls. Canadian Geotechnical Journal, 2003, 40(5): 976−994
20. Bathurst R J, Allen T M, Walters D L. Reinforcement loads in geosynthetic walls and the case for a new working stress design method. Geotextiles and Geomembranes, 2005, 23(4): 287−322
21. Ling H I, Tatsuoka F, Tateyama M. Simulating performance of GRS-RW by finite-element procedure. Journal of Geotechnical Engineering, 1995, 121(4): 330−340
22. Liu H, Ling H I. A unified elastoplastic-viscoplastic bounding surface model of geosynthetics and its applications to geosynthetic reinforced soil-retaining wall analysis. Journal of Engineering Mechanics, 2007, 133(7): 801−815
23. Bathurst R J, Cai Z. Pseudo-static seismic analysis of geosynthetic-reinforced segmental retaining walls. Geosynthetics International, 1995, 2(5): 787−830
24. Gao Y F, Yang S C, Wu Y X, Li D Y, Zhang F. Evaluation of oblique pullout resistance of reinforcements in soil wall subjected to seismic loads. Geotextiles and Geomembranes, 2014, 42(5): 515−524
25. Ling H I, Leshchinsky D. Effects of vertical acceleration on seismic design of geosynthetic-reinforced soil structures. Geotechnique, 1998, 48(3): 347−373
26. Yang S C, Gao Y F, Cui K, Zhang F, Wu D. Three-dimensional internal stability analysis of geosynthetic-reinforced earth structures considering seismic loading. Soil Dynamics and Earthquake Engineering, 2020, 130: 105979
27. Mohamed S B A, Yang K H, Hung W Y. Limit equilibrium analyses of geosynthetic-reinforced two-tiered walls: Calibration from centrifuge tests. Geotextiles and Geomembranes, 2013, 41: 1−16
28. Sabermahani M, Ghalandarzadeh A, Fakher A. Experimental study on seismic deformation modes of reinforced-soil walls. Geotextiles and Geomembranes, 2009, 27(2): 121−136
29. Cai Z, Bathurst R J. Seismic response analysis of geosynthetic reinforced soil segmental retaining walls by finite element method. Computers and Geotechnics, 1995, 17(4): 523−546
30. Ren F, Zhang F, Xu C, Wang G. Seismic evaluation of reinforced-soil segmental retaining walls. Geotextiles and Geomembranes, 2016, 44(4): 604−614
31. Fan C, Liu H, Cao J, Ling H I. Responses of reinforced soil retaining walls subjected to horizontal and vertical seismic loadings. Soil Dynamics and Earthquake Engineering, 2020, 129: 105969
32. Leshchinsky D, Kang B, Han J, Ling H I. Framework for limit state design of geosynthetic-reinforced walls and slopes. Transportation Infrastructure Geotechnology, 2014, 1(2): 129−164
33. Leshchinsky D, Leshchinsky B, Leshchinsky O. Limit state design framework for geosynthetic-reinforced soil structures. Geotextiles and Geomembranes, 2017, 45(6): 642−652
34. Ling H I, Leshchinsky D. Failure analysis of modular-block reinforced-soil walls during earthquakes. Journal of Performance of Constructed Facilities, 2005, 19(2): 117−123
35. Mohamed S B A, Yang K H, Hung W Y. Finite element analyses of two-tier geosynthetic-reinforced soil walls: Comparison involving centrifuge tests and limit equilibrium results. Computers and Geotechnics, 2014, 61: 67−84
36. Liu H. Internal stability analysis of segmental geosynthetic-reinforced soil retaining walls subjected to seismic loading. Chinese Journal of Geotechnical Engineering, 2008, 30(2): 278−283 (in Chinese)
37. Zhou Y D, Zhang F, Wang J Q, Gao Y F, Dai G Y. Seismic stability of earth slopes with tension crack. Frontiers of Structural and Civil Engineering, 2019, 13(4): 950−964
38. Yang S C, Leshchinsky B, Cui K, Zhang F, Gao Y F. Influence of failure mechanism on seismic bearing capacity factors for shallow foundations near slopes. Geotechnique, 2021, 71(7): 594−607
39. Yang S C, Leshchinsky B, Cui K, Zhang F, Gao Y F. Unified approach toward evaluating bearing capacity of shallow foundations near slopes. Journal of Geotechnical and Geoenvironmental Engineering, 2019, 145(12): 04019110
40. Zhou Z, Gao Y F, Zhang F, Song J, Zou D G. Effects of soil dynamic response on post-earthquake deformation of slopes based on nested Newmark model. Earthquake Engineering and Engineering Vibration, 2020, 19(3): 573−582
41. Zhou Z, Zhang F, Gao Y F, Shu S. Nested Newmark model to estimate permanent displacement of seismic slopes with tensile strength cut-off. Journal of Central South University, 2019, 26(7): 1830−1839
42. Zhuang X Y, Zhou S W, Sheng M, Li G S. On the hydraulic fracturing in naturally-layered porous media using the phase field method. Engineering Geology, 2020, 266: 105306
43. Zhou S W, Zhuang X Y, Rabczuk T. Phase field modeling of brittle compressive-shear fractures in rock-like materials: A new driving force and a hybrid formulation. Computer Methods in Applied Mechanics and Engineering, 2019, 355: 729−752
44. Zhou S W, Zhuang X Y, Zhu H H, Rabczuk T. Phase field modelling of crack propagation, branching and coalescence in rocks. Theoretical and Applied Fracture Mechanics, 2018, 96: 174−192